Spatial/temporal photocurrent and electronic transport in monolayer molybdenum disulfide grown by chemical vapor deposition

Zhengfeng Yang, Roberto Grassi, Marcus Freitag, Yi-Hsien Lee, Tony Low, and Wenjuan Zhu

---

Articles you may be interested in

2D-2D tunneling field-effect transistors using WSe_2/$SnSe_2$ heterostructures
Applied Physics Letters **108**, 083111 (2016); 10.1063/1.4942647

Chemical vapor deposition of monolayer MoS_2 directly on ultrathin Al_2O_3 for low-power electronics
Applied Physics Letters **110**, 053101 (2017); 10.1063/1.4975064

Ferroelectric transistors with monolayer molybdenum disulfide and ultra-thin aluminum-doped hafnium oxide
Applied Physics Letters **111**, 013103 (2017); 10.1063/1.4991877

Band offsets and heterostructures of two-dimensional semiconductors
Applied Physics Letters **102**, 012111 (2013); 10.1063/1.4774090

p-type doping of MoS_2 thin films using Nb
Applied Physics Letters **104**, 092104 (2014); 10.1063/1.4867197

Band alignment of two-dimensional transition metal dichalcogenides: Application in tunnel field effect transistors
Applied Physics Letters **103**, 053513 (2013); 10.1063/1.4817409

Spatial/temporal photocurrent and electronic transport in monolayer molybdenum disulfide grown by chemical vapor deposition

Zhengfeng Yang,[1] Roberto Grassi,[2] Marcus Freitag,[3] Yi-Hsien Lee,[4] Tony Low,[2] and Wenjuan Zhu[1,a)]

[1]*Electrical and Computer Engineering, University of Illinois at Urbana-Champaign, Urbana, Illinois 61801, USA*
[2]*Department of Electrical & Computer Engineering, University of Minnesota, Minneapolis, Minnesota 55455, USA*
[3]*IBM Thomas J. Watson Research Center, Yorktown Heights, New York 10598, USA*
[4]*Department of Materials Science and Engineering, National Tsing Hua University, Hsinchu, Taiwan 30013*

We systematically investigate the spatial/temporal photocurrent in photodetectors and electronic transport in transistors/Hall-bar devices based on monolayer MoS_2 grown by chemical vapor deposition (CVD). We found that the maximum photocurrent occurs when the laser spot is close to the metal/MoS_2 contact and is tunable by the applied drain voltage, which can be explained by the modulation of the local electric field at the Schottky barrier, consistent with predictions from our quantum transport simulation. We observed that the maximum photocurrent at drain contact is much larger than the one at the source contact, and the DC currents show rectifying behavior. These phenomena can be explained by the different Schottky barrier heights at the two contacts. By measuring Hall-bar structure at various temperatures from 100 K to 400 K, we extracted the barrier heights at the source and drain contacts, separately. We found that the barrier height at drain contact is about 50 mV larger than the one at the source contact, consistent with the photocurrent and DC current observations. We measured the photocurrent at various powers, and a photoresponsivity of 3.07 mA/W was extracted at low powers. When the power increases above 20 μW, the photocurrent starts to saturate. Temporal response of the photocurrent is also dependent on the laser power. At high laser powers, photocurrent overshoot was observed. The photocurrent saturation at high powers and the overshoot in temporal photocurrent are likely due to the same mechanism: an accumulation of electrons in the channel, flattening out the band structure, since the laser spot is located near the drain contact in these measurements. These studies of photocurrents and electronic transport in CVD MoS_2 highlight the importance of the contacts in the electronic/optoelectronic devices and reveal the physical mechanism of the photocurrent/electronic transport in these devices. © 2016 AIP Publishing LLC. [http://dx.doi.org/10.1063/1.4942508]

Beyond graphene, transition metal dichalcogenide (TMD) layered materials are attracting intense research interest due to their appreciable bandgap in the visible and unique electronics,[1,2] optical,[3] and mechanical properties.[4] MoS_2 is the most commonly studied member of TMD,[5] exhibiting an indirect bulk bandgap of 1.3 eV that turns into a direct bandgap of 1.8 eV when thinned down to its monolayer.[6] The direct bandgap in monolayer MoS_2 enables a suite of optical applications such as photodetector[7–9] and photovoltaics.[10,11] High photo-responsivity of monolayer or multilayer MoS_2,[12,13] strong light–matter interaction in TMD heterostructures,[14] and plasmon enhanced or dye-sensitized photodetector[15] have been demonstrated. These encouraging reports coupled with continual engineering efforts[2,16] present a compelling case for monolayer MoS_2 as a candidate for optoelectronics in the visible spectrum. Recently, the advent of mass production technologies has enabled scalable growth of polycrystalline monolayer MoS_2 by chemical vapor deposition (CVD),[17] hence providing a commercially viable path towards MoS_2 optoelectronics at low cost.[18] Although there are several works that discuss the photocurrent mechanisms in MoS_2 transistor,[9,10,12,19] different origins due to thermoelectric[10] and photovoltaic[9,12] effects were reported, and the dominating mechanism depends also on the device structure and its material. In this paper, we systematically studied the mechanisms of photoresponse in CVD grown MoS_2 through its spatial and temporal photocurrent. We found that the photocurrent is dominated by photovoltaic effect at the metal-semiconductor Schottky junction, and the photocurrent polarity and magnitude were found to be strongly tunable with the applied drain and gate voltages. These trends can be explained by the local band bending at the Schottky junction, consistent with the quantum transport simulations. We found asymmetric photocurrent at the source and drain contacts ascribed to the different contact barrier height. An extracted barrier height of 107 mV at the drain contact is about 50 mV larger than the one at the source contact.

Figs. 1(a) and 1(b) show the schematic and scanning electron microscopy (SEM) image of the MoS_2 based photodetector. The photoresponse of monolayer CVD MoS_2 is measured using scanning photocurrent microscopy. Fig. 1(c) shows the spatially resolved photocurrent at various drain voltages. The line profile of the photocurrent is shown in
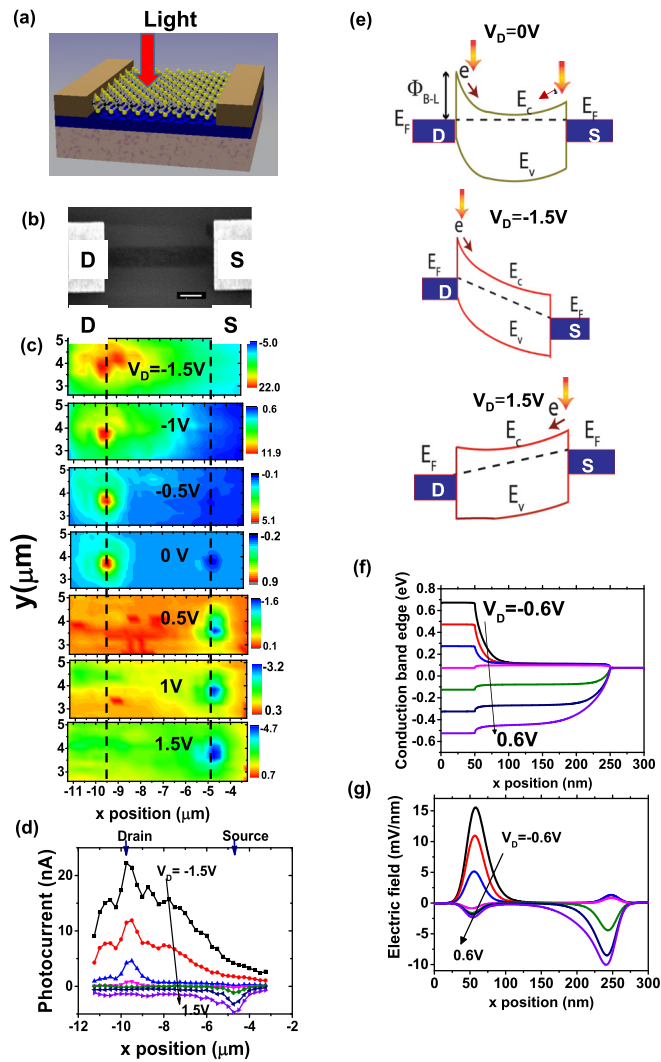
a)wjzhu@illinois.edu

FIG. 1. (a) Illustration of MoS$_2$ based photodetector. (b) SEM of the MoS$_2$ photodetector. The scale bar is 1 μm. The MoS$_2$ channel width is 1 μm and length is 5 μm. (c) Spatially resolved photocurrent at various drain voltages. The dashed lines are for guiding eyes to highlight the position of the source and drain contact edge. (d) Line profile of the photocurrent along the channel. (e) Illustration of the energy band diagram. (f) and (g) are modeling results. (f) Conduction band edge profile $E_c(x)$ at $V_g = 1$ V and various drain voltages. The simulated device has a channel length of 200 nm, and top source and drain contacts with a length of 50 nm (the channel extends from $x = 50$ to $x = 250$ nm). The Fermi level of the source (right contact) is taken as the reference energy. (g) Corresponding electric field profile $-dE_c/dx$ smoothed through a Gaussian function with a standard deviation of 10 nm.

Fig. 1(d). When the drain voltage is zero, there are two local maxima in the photocurrent, located at the source and drain contact, respectively. This is because the Schottky barrier at the contacts results in two local maxima in band bending, i.e., maximum local electric field, as illustrated in Fig. 1(e). The photon generated electron-hole pairs can be most efficiently separated and swept to the electrode. Note that the thermoelectric effect gives the same current direction as photovoltaic effect at zero drain bias. When drain voltage is increasingly negative, the maximum photocurrent located at the drain contact increases, while the maximum photocurrent at the source contact decreases. This can be explained by the band diagram shown in Fig. 1(e). When the drain voltage is negative, the band bending at the drain increases resulting in higher photocurrent, while the band bending at the source is

reduced, which suppresses the photocurrent. Similarly, when the drain voltage is positive, the photocurrent at the source contact is enhanced, while the one at the drain contact is suppressed. The fact that the photocurrents change sign as the drain voltage changes polarity indicates that photovoltaic effect dominates over the thermoelectric effect at these drain bias conditions. Since our device is operating in the unipolar regime, the sign of the Seebeck coefficient in the MoS$_2$ channel does not change with bias conditions. Hence, the photothermoelectric will predict no change in polarity contrary to experimental observations.

This photocurrent mechanism is also consistent with the gate voltage dependent results, as shown in Fig. S1 (see supplementary materials[20]). When gate voltage is more positive, i.e., the channel is biased toward accumulation, the band bending at the contacts increases, resulting in a higher photocurrent. On the other hand, when gate voltage modulates the channel towards depletion, the band bending is reduced at the contact, resulting in a lower photocurrent. In addition, when the channel is in accumulation, the total resistance between the contacts is lower, which can also result in a higher photocurrent.

In order to support the above considerations, we have performed a numerical simulation of a device with 200-nm channel length and similar structure (top source and drain contacts, back gate, and 90-nm thick SiO$_2$ dielectric) using a self-consistent ballistic quantum transport solver based on the non-equilibrium Green's function formalism.[21] An effective mass Hamiltonian is employed to describe the K-valley conduction band electrons. Injection from the source and drain contacts is treated through a phenomenological self-energy (see supplementary materials[20]), and a fixed Schottky barrier height of 75 mV is assumed for both contacts. The shape of the band profiles shown in Fig. 1(f) for varying drain voltage, and in Fig. S1(d) (see supplementary materials[20]) for varying gate voltage, confirms the trends observed experimentally: when changing the drain voltage from negative to positive values, the location of the maximum band bending moves from drain to source; also, the band bending at the source side increases with increasing V_g. Indeed, the extracted electric field profiles in Fig. 1(g) and S1(e) (see supplementary materials[20]) qualitatively resemble the plots of the spatially resolved photocurrent in Fig. 1(c) and Fig. S1(a) (see supplementary materials[20]). A notable difference compared to experiments is that the electric field in the middle of the channel tends to go to zero for low V_D or high V_G, an effect which is related to the ballistic transport assumption. We also found a stronger gate tunability in simulation compared to counterpart experimental devices, which is probably due to the presence of significant trap states density in our devices.[22]

In Fig. 1, we also observed that at the same $|V_D|$, the photocurrent at the drain side is much higher than at the source side, indicating asymmetric barriers at the source and drain contacts, with higher slope at the drain side. The asymmetric barrier may come from non-uniform doping or density of surface states in transferred CVD MoS$_2$ film. Different doping in MoS$_2$ at two contact region will result in different work function in MoS$_2$, i.e., different band bending near the contacts. Then, the local electric field near one

contact will be different from the other contact. The asymmetric barriers can also be due to the spatial variation of interface states. Since the Fermi level in semiconductor can be pinned by the high density of surface states, the band bending in semiconductor will be influenced not only by the metal semiconductor work function difference but also the density of interface states at the contact.[23] These interface states can come from the lattice defects such as sulfur vacancy, impurities on the surface, KOH residuals used for film transfer, or perylene-3,4,9,10-tetracarboxylic acid tetrapotassium salt (PTAS) seeds used for MoS$_2$ growth.

This asymmetric band bending is also reflected in the DC I$_D$-V$_D$ characteristics. Figs. 2(a) and 2(b) show the I$_D$-V$_D$ measurement at two different configurations as the insets illustrate; the drain voltage is applied on the left and right electrodes, respectively. We see a rectifying behavior of the drain current even when the gate voltage is zero. Figs. 2(c) and 2(d) illustrate the band diagram and the drain current at various bias conditions. When the voltage on the left contact is higher than the one on the right, electrons are injected from the right contact, corresponding to the bias configurations B and C. Conversely, when the voltage on the left contact is lower than the one on the right, electrons are injected from the left contact, corresponding to the bias configurations A and D. The fact that the currents in case B and C are much higher than in case A and D indicate that the effective barrier height on the left is much larger than the one on the right and that the transistor acts as a Schottky-barrier transistor. This is consistent with the asymmetric photocurrent results discussed previously.

To quantify the asymmetric Schottky barrier heights at the source and drain contacts, a Hall-bar top-gated device based on CVD MoS$_2$ is measured at various temperatures and drain voltages to extract the Schottky barrier heights at the source and drain contacts, respectively. The inset of Fig. 3(a) shows the layout of a Hall-bar device. Four-point resistance was measured, shown in Fig. S2 (see supplementary materials[20]). The total resistance and the resistance between two sensing terminals at various temperatures are shown in Fig. S2 (see supplementary materials[20]). The voltage

dropped on each contact can be extracted by plotting the electrostatic potential along the channel, illustrated in the inset of Fig. 3(a). From the slope of curve between sensing terminal 1 and 2, we can extract the channel sheet resistance. From the potential drop between source (drain) and sensing terminal 1(2) and sheet resistance of the channel, we can extract the voltage dropped on source (drain) contact. Taking into account the polarity of voltage drop at two contacts, the extracted contact resistance at the source contact (R$_s$) with V$_D$ = −0.1 V and drain contact (R$_d$) with V$_D$ = 0.1 V at various gate voltages and temperatures is shown in Fig. S2(d) (see supplementary materials[20]). At a given temperature, R$_d$ is nearly an order of magnitude larger than R$_s$. The Schottky thermal emission current at the contact can be expressed as[24,25]

$$J \propto T^{\frac{3}{2}} \times \exp\left(-\frac{q\varphi_B}{K_B T}\right)\left[\exp\left(\frac{qV(T)}{K_B T}\right) - 1\right], \quad (1)$$

where φ_B is the barrier height between MoS$_2$ and the metal contact, $V(T)$ is the voltage drop at the contact, K_B is the Boltzmann constant, and T is the temperature. Note that since voltage drop $V(T)$ at both contacts reveals a temperature-dependent behavior, a linear approximation equation $V(T) = V_0 + b \cdot T$ is applied, where V_0 and b are fitting parameters. The power law of T$^{3/2}$ comes from the Boltzmann carrier distribution and the thermal velocity. It is less than T^2 commonly found in a 3D system because of the constant value of the density-of-states in a 2D system. The contact resistance dominated by Schottky thermal emission can be expressed as

$$R_c = \left(\frac{\partial J}{\partial V}\right)^{-1} \propto T^{-1/2} \times \exp\left(\frac{q(\varphi_B - V_0)}{K_B T}\right). \quad (2)$$

Fig. 3(b) plots $\ln(R_c * T^{1/2})$ as a function of $1000/T$ for both contacts. From the slope of the plot, the barrier heights could be extracted at the source and drain contacts, respectively. Fig. 3(c) shows the extracted barrier heights differently at both contacts at various top gate voltages. A barrier height of 107 mV is extracted at the drain contact, which is
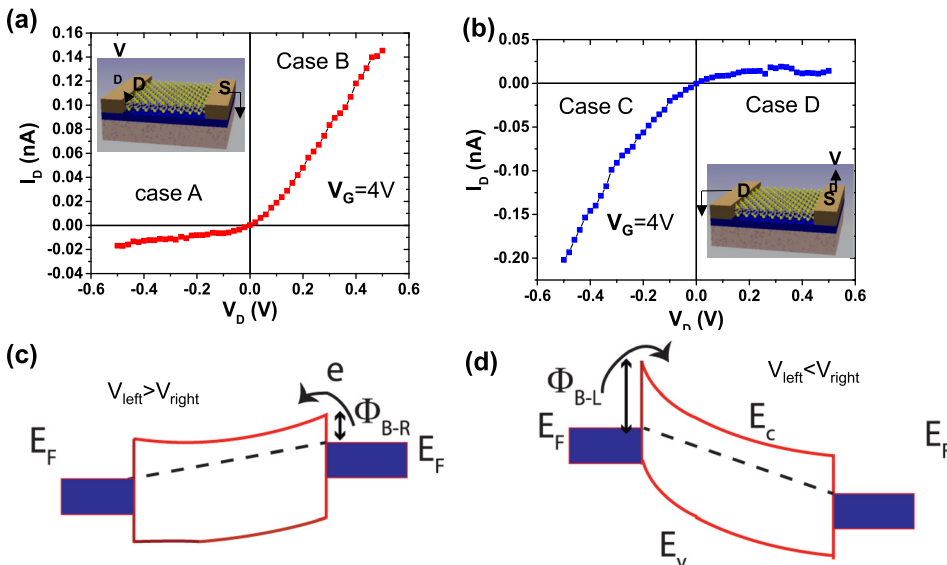

(a)

(b)

(c)

(d)

FIG. 2. (a) and (b) I$_D$-V$_D$ characteristics at two different configurations illustrated in the insets: the drain voltage is applied on the left and right electrodes, respectively. (c) and (d) illustrate the band diagram and the drain current at two different bias conditions.
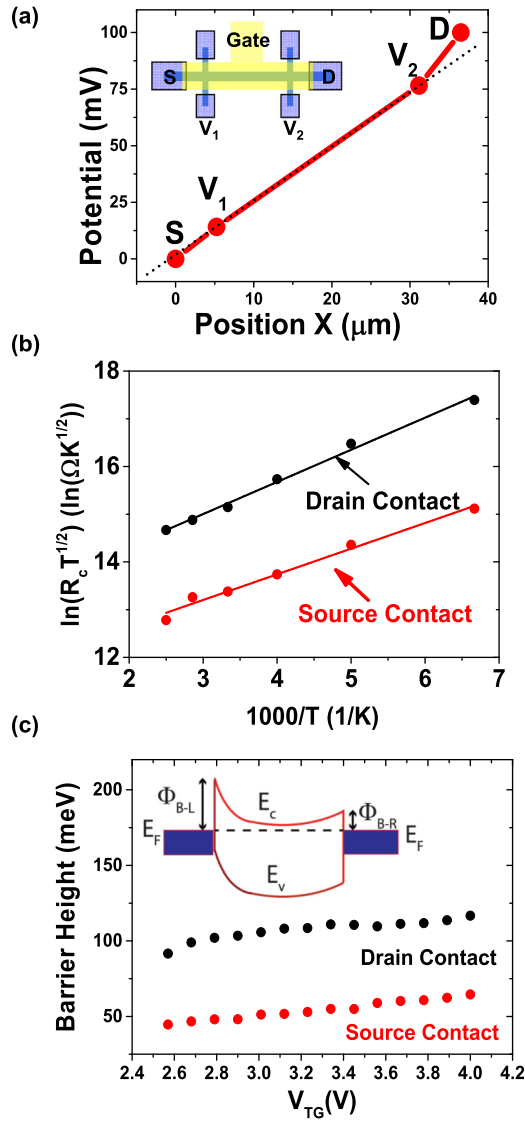
FIG. 3. (a) Potential as a function of position along the channel from the source, sensing terminal 1, sensing terminal 2 to the drain contact, when 0.1 V bias is applied to drain contact at 300 k with $V_{TG} = 3.0$ V. The inset illustrates the layout of the Hall-bar device. (b) $\ln(R_c T^{0.5})$ as a function of $1000/T$ when V_D is applied to drain contact at $V_{TG} = 3.0$ V. The black and red points denote drain contact with $V_D = 0.1$ V and source contact with $V_D = -0.1$ V, respectively. Inset: (c) Extracted barrier heights at the drain contact (black points) and source contact (red points) at various top gate voltages. Inset: Illustration of different barrier heights at the drain and source contacts.

about 50 mV larger than the one at the source contact. This pronounced difference in barrier heights at two contacts, illustrated in the inset of Fig. 3(c), explains the asymmetric photocurrent and DC current results discussed previously.

The temporal response of the photocurrent is measured by using a mechanical chopper and oscilloscope. Fig. 4(a) shows the transit photocurrent as a function of time at various laser powers. The response time of this ac photocurrent is on the order of milliseconds or less, which is much shorter than the one in DC photocurrent reported earlier. The reason is that the change of DC photocurrent is mainly due to the "photogating" effect caused by charge trapping in the gate dielectrics, while the change of ac photocurrent is mainly caused by the change of conductivities due to the photoinduced carriers. The carrier generation/recombination process
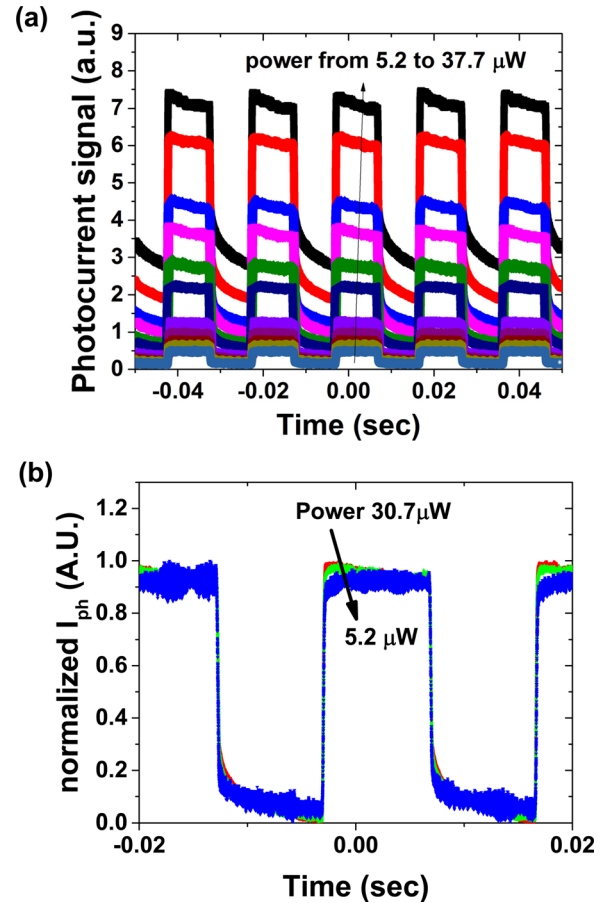

FIG. 4. (a) Transit photocurrent of MoS$_2$ photodetector as a function of time at various laser powers. (b) Zoom in comparison of three different power levels. The graphs are rescaled and shifted for comparison.

is typically much faster than the charge trapping process. As the light power increases, the photocurrent increases, due to the larger generation of electron–hole pairs. Another interesting feature we noticed is that the photocurrent has an overshoot when light is turned on and gradually goes back to a steady state. Fig. 4(b) shows the zoom in comparison of three different power levels. The graphs are rescaled and shifted for comparison. We can see that the higher the power, the larger the overshoot. When power is at 18.5 μW or below, the overshoot is nearly negligible.

The photoresponsivity is measured by varying the laser power, as shown in Fig. S3 (see supplementary materials[20]). We can see that the photocurrent increases as power increases. From this, we extrapolate the photoresponsivity as 3.07 mA/W. This is comparable to the results reported on other MoS$_2$ photodetectors.[8,9,12,24,26] When the power increases above 20 μW, the photocurrent starts to saturate. The power level where saturation sets in coincides with the power level where the overshoot starts to happen in chopped measurements, and the two observations likely are due to the same mechanism. Possibilities include (1) an accumulation of electrons in the channel, flattening out the band structure (Since the laser spot is located near the drain contact with $V_D = -1.5$ V, holes can immediately reach drain electrode, while the electron needs to travel through the entire channel to reach the source electrode, resulting in accumulation of electrons in the channel.), (2) trapping of photo-generated

carriers, which gates the transistor more towards depletion, or (3) a saturation of the absorption due to band filling of available electronic states.

In summary, spatial and temporal photocurrents and contact resistance at various temperatures were systematically studied in CVD MoS_2 based photodetector and Hall-bar devices. We find that the maximum photocurrent occurred at the metal/semiconductor contacts, due to the Schottky barrier and the resulting maximum local electric field. The amplitude and location of the maximum photocurrent were modulated by the drain and gate voltage, consistent with our numerical simulation. Asymmetric behavior is observed in photocurrent and DC characterization, indicating different barrier heights at the source and drain contacts. By measuring the four-point resistance at various temperatures and drain voltages, we were able to extract the barrier heights at the source and drain contacts, respectively, and found that the barrier height at the drain contact is about 50 mV larger than the one at the source contact. The asymmetric barrier heights at the two contacts may come from inhomogenous doping and/or interface state density in CVD MoS_2. These findings will be valuable for future photodetectors based on transition metal dichalcogenides.

Methods: Large-scale monolayer MoS_2 was synthesized at 650 °C by atmospheric pressure chemical vapor deposition (APCVD) using PTAS as the seed on SiO_2/Si substrate.[27] Sulphur powder and molybdenum oxide (MoO_3) were used as the precursors for the synthesis. Then, MoS_2 is transferred to a fresh SiO2/Si substrate using KOH solution. Source/drain contacts are formed by ebeam lithography and metal evaporation. The electrode is composed of Ti/Au. The MoS_2 channel is patterned by lithography and O_2 plasma etching. The top gate dielectric comprised an AlOx/HfO_2 stack. The AlOx was formed by electron beam evaporation of 2 nm of aluminum metal followed by its natural oxidization in air for a few hours. The 30 nm thick HfO_2 layer was formed using atomic layer deposition (ALD) at 170°. The top gate electrode of Hall-bar device for barrier height measurement was Ti/Au (5/40 nm). Fig. 1(a) illustrated the structure of MoS_2 based photodetector. He-Ne laser is used as the light source. Light is modulated by the mechanical chopper. The photocurrent is amplified by the pre-amplifier and measured by the lock-in amplifier.

[1]B. Radisavljevic, A. Radenovic, J. Brivio, V. Giacometti, and A. Kis, Nat. Nanotechnol. **6**(3), 147 (2011).

[2]X. Cui, G.-H. Lee, Y. D. Kim, G. Arefe, P. Y. Huang, C.-H. Lee, D. A. Chenet, X. Zhang, L. Wang, F. Ye, F. Pizzocchero, B. S. Jessen, K. Watanabe, T. Taniguchi, D. A. Muller, T. Low, P. Kim, and J. Hone, Nat. Nanotechnol. **10**(6), 534 (2015).

[3]M. K. Fai, L. Changgu, H. James, S. Jie, and F. Heinz Tony, Phys. Rev. Lett. **105**(13), 136805 (2010); D. Xiao, G.-B. Liu, W. Feng, X. Xu, and W. Yao, Phys. Rev. Lett. **108**(19), 196802 (2012).

[4]I. Kaplan-Ashiri and S. R. Cohen, Proc. Natl. Acad. Sci. **103**, 523 (2006); S. Bertolazzi, J. Brivio, and A. Kis, ACS Nano **5**, 9703 (2011); J. Pu, Y.

[5]Yomogida, K. K. Liu, L. J. Li, and Y. Iwasa, Nano Lett. **12**(8), 4013 (2012); W. Wu, L. Wang, Y. Li, F. Zhang, L. Lin, S. Niu, and D. Chenet, Nature **514**, 470 (2014).

[5]P. Joensen, R. F. Frindt, and S. Roy Morrison, Mater. Res. Bull. **21**(4), 457 (1986).

[6]A. Kuc, N. Zibouche, and T. Heine, Phys. Rev. B **83**, 245213 (2011).

[7]R. S. Sundaram, M. Engel, A. Lombardo, R. Krupke, A. C. Ferrari, Ph. Avouris, and M. Steiner, Nano Lett. **13**, 1416 (2013); C. C. Wu, D. Jariwala, and V. K. Sangwan, J. Phys. Chem. Lett. **4**(15), 2508 (2013).

[8]H. S. Lee, S. W. Min, Y. G. Chang, M. K. Park, and T. Nam, Nano Lett. **12**(7), 3695 (2012).

[9]Z. Yin, H. Li, H. Li, L. Jiang, Y. Shi, Y. Sun, G. Lu, Q. Zhang, X. Chen, and H. Zhang, ACS Nano **6**(1), 74 (2012).

[10]M. Buscema, M. Barkelid, V. Zwiller, and H. S. J. van der Zant, Nano Lett. **13**(2), 358 (2013).

[11]A. Pospischil, M. M. Furchi, and T. Mueller, Nat. Nano **9**(4), 257 (2014); A. Dashora, U. Ahuja, and K. Venugopalan, Comput. Mater. Sci. **69**, 216 (2013).

[12]L.-S. Oriol, L. Dominik, K. Metin, R. Aleksandra, and K. Andras, Nat. Nanotechnol. **8**(7), 497 (2013).

[13]D. Tsai, D. Lien, M. Tsai, S. Su, K. Chen, J. Ke, Y. Yu, L. Li, and J. He, IEEE J. Sel. Top. Quantum Electron. **20**(1), 3800206 (2014).

[14]L. Britnell, R. M. Ribeiro, A. Eckmann, R. Jalil, B. D. Belle, A. Mishchenko, Y. J. J. Kim, R. V. Gorbachev, T. Georgiou, S. V. Morozov, A. N. Grigorenko, A. K. Geim, C. Casiraghi, A. H. Castro Neto, and K. S. Novoselov, Science **340**(6138), 1311 (2013); N. Huo, J. Kang, Z. Wei, S. S. Li, and J. Li, Adv. Funct. Mater. **24**(44), 7025 (2014); W. Zhang, C. P. Chuu, J. K. Huang, C. H. Chen, and M. L. Tsai, Sci. Rep. **4**, 3826 (2014).

[15]C.-H. Lee, G.-H. Lee, A. M. van der Zande, W. Chen, Y. Li, M. Han, X. Cui, G. Arefe, C. Nuckolls, T. F. Heinz, J. Guo, J. Hone, and P. Kim, Nat. Nano **9**(9), 676 (2014); S. H. Yu, Y. Lee, S. K. Jang, J. Kang, J. Jeon, C. Lee, J. Y. Lee, H. Kim, E. Hwang, S. Lee, and J. H. Cho, ACS Nano **8**(8), 8285 (2014).

[16]S. Das, H.-Y. Chen, A. V. Penumatcha, and J. Appenzeller, Nano Lett. **13**(1), 100 (2013).

[17]K. K. Liu, W. Zhang, Y. H. Lee, Y. C. Lin, and M. T. Chang, Nano Lett. **12**(3), 1538 (2012); S. Najmaei, Z. Liu, W. Zhou, X. Zou, G. Shi, and S. Lei, Nat. Mater. **12**, 754 (2013); Y.-H. Lee, X.-Q. Zhang, Z. Wenjing, M.-T. Chang, L. Cheng-Te, K.-D. Chang, Y. Y.-Chu, T. Wang Jacob, C.-S. Chang, L.-J. Li, and T.-W. Lin, Adv. Mater. **24**(17), 2320 (2012); Y. Zhan, Z. Liu, S. Najmaei, P. M. Ajayan, and J. Lou, Small **8**(7), 966 (2012).

[18]H. Wang, L. Yu, Y. H. Lee, W. Fang, and A. Hsu, in IEEE International Electron Devices Meeting (IEDM) (2012), p. 4.6.1; N. Perea-López, Z. Lin, and N. R. Pradhan, 2D Mater. **1**, 011004 (2014).

[19]Y. Zhang, H. Li, L. Wang, H. Wang, X. Xie, and S. L. Zhang, Sci. Rep. **5**, 7938 (2015).

[20]See supplementary material at http://dx.doi.org/10.1063/1.4942508 for figures of gate voltage tuned spatially resolved photocurrent and corresponding modeling results, the MoS_2 based Hall-bar device resistance measured at various temperatures, photocurrent measured at various laser power, more details on the numerical simulation of MoS_2 photodetector.

[21]S. Datta, Quantum Transport: Atom to Transistor (Cambridge University Press, 2005).

[22]W. Zhu, T. Low, Y.-H. H. Lee, H. Wang, D. B. Farmer, J. Kong, F. Xia, and P. Avouris, Nat. Commun. **5**, 3087 (2014).

[23]R. Muller and T. Kamins, Device Electronics for Integrated Circuits, 3rd ed. (Wiley, New York, 2002).

[24]G. Cunningham, D. Hanlon, N. McEvoy, and G. S. Duesberg, Nanoscale **7**, 198 (2015).

[25]L. L. Yu, Y. H. Lee, X. Ling, E. J. G. Santos, Y. C. Shin, Y. X. Lin, M. Dubey, E. Kaxiras, J. Kong, H. Wang, and T. Palacios, Nano Lett. **14**(6), 3055 (2014).

[26]W. Zhang, J. K. Huang, C. H. Chen, and Y. H. Chang, Adv. Mater. **25**(25), 3456 (2013); Y. W. Jong, L. Yuan, Z. Hailong, Y. Anxiang, L. Zheng, H. Yu, and D. Xiangfeng, Nat. Nanotechnol. **8**(12), 952 (2013); M. M. Furchi, D. K. Polyushkin, A. Pospischil, and T. Mueller, Nano Lett. **14**(11), 6165 (2014); W. Choi, M. Y. Cho, A. Konar, J. H. Lee, and G. B. Cha, Adv. Mater. **24**(43), 5832 (2012).

[27]Y.-H. H. Lee, L. Yu, H. Wang, W. Fang, X. Ling, Y. Shi, C.-T. T. Lin, J.-K. K. Huang, M.-T. T. Chang, C.-S. S. Chang, M. Dresselhaus, T. Palacios, L.-J. J. Li, and J. Kong, Nano Lett. **13**(4), 1852 (2013).